ORIGINAL PAPER

The Structure of Mixed Mn–Co Oxide Catalysts for CO Oxidation

O. A. Bulavchenko[1,2] · T. N. Afonasenko[3] · S. S. Sigaeva[3] · A. V. Ivanchikova[1,2] · A. A. Saraev[1,2] ·
E. Yu. Gerasimov[1,2] · V. V. Kaichev[1,2] · S. V. Tsybulya[1,2]

Abstract

A series of $Mn_5Co_1O_x$ catalysts calcined at different temperatures in the range of 400–800 °C were synthesized by coprecipitation of manganese and cobalt nitrates and tested in the oxidation of CO. The specific surface area, structure, and chemistry of the catalysts were studied. In addition, the reduction of the catalysts by hydrogen was studied using in situ X-ray diffraction and temperature-programmed reduction techniques. It was found that the low-temperature catalyst calcined at 400 °C displays the best catalytic activity, which is attributed to its high surface area, low-temperature reducibility, and a high surface content of Mn^{4+}. The formation of highly disperse and active $CoMnO_3$ species and excess oxygen in a $Mn_{3-x}Co_xO_{4+\delta}$ spinel leads to excellent low-temperature redox properties. The elevated temperature calcination results in a decline in the catalytic activity in CO oxidation due to formation of a well crystalline $Mn_{3-x}Co_xO_4$ spinel, a decrease in the surface area and reducibility.

Keywords Heterogeneous catalysts · CO oxidation · Mn oxide · Co oxide · Solid solution · Mn–Co mixed oxides

1 Introduction

Volatile organic compounds (VOCs) and CO emitted from industry and transport are harmful to environment and human health [1]. Catalytic total oxidation is an efficient way for exhaust gases purification due to relatively low processing temperature, high burning efficiency and sustainability. The noble metal catalysts (Pt, Pd, and Ag) are the most active in the total oxidation [2, 3]; however, they have disadvantages such as a high price, easy sintering, coking, and poisoning, which limit their wide application [4]. On the other hand, transition metal oxides (CoO_x, FeO_x, MnO_x, etc.) are thermostable, resistant to poisons and have a very low price, but they exhibited relatively poor catalytic performance [5, 6]. One way to improve the catalytic performance is the use of composite transition metal oxides, which usually exhibit superior catalytic activity as compared to those of individual oxides, due to the synergetic effect [7].

Manganese oxides are known to have moderate activity in oxidation reactions owing to the flexible valence states (MnO_2, Mn_2O_3, Mn_3O_4, and MnO), reducibility and oxygen mobility [8]. Manganese oxide is capable of interacting with other elements to form solid solutions and new compounds. Among Mn-based mixed oxides, Mn–Co oxide catalysts are of interest for a wide catalytic application including VOCs [9–15] and CO oxidation [16, 17]. For example, Kovanda et al. [14] found that an increase in catalytic activity in the ethanol oxidation over Co–Mn catalysts is caused by an increase in the number of easily reducible sites and weakly bound oxygen. Aguilera et al. [15] showed that Mn–Co mixed oxides have superior catalytic properties in the oxidation of toluene, ethanol, and butanol due to generation of amorphous phases. On the other hand, Tang et al. [11] found that the formation of a Mn–Co solid solution with a spinel structure inhibits the growth of nanoparticles, which leads to an increase in surface area, and the strong synergistic effect of Mn and Co in oxide contributes greatly to its low-temperature reducibility, which plays a key role in the VOCs oxidation.

The most active Co–Mn catalysts were obtained at relatively low temperatures of 300–400 °C [10, 16–18]; therefore, it is difficult to precisely determine the origin of

✉ O. A. Bulavchenko
isizy@catalysis.ru

1 Boreskov Institute of Catalysis SB RAS, Lavrentiev Ave., 5, Novosibirsk, Russia 630090

2 Novosibirsk State University, Pirogova Str., 2, Novosibirsk, Russia 630090

3 Center of New Chemical Technologies BIC, Neftezavodskaya, 54, Omsk, Russia 644040

active phase. During low-temperature synthesis, incomplete interaction between elements can occur and lead to the formation of amorphous or highly disperse phases. Recently, Zhang et al. [10] investigated the influence of calcination temperature on the catalyst structure for a Co-rich oxide ($Co_2Mn_1O_x$). It was found that superior catalytic performance in total oxidation is associated with the formation of a poorly crystalline spinel having a large surface area, good low-temperature redox properties, and abundant active oxygen species. To the best of our knowledge, most research of Co–Mn catalysts are focused on the systems with an excess of Co rather than Mn, and the structure–activity relationship was not systematically established using the variation of calcination temperature for the Mn-rich catalysts. The purpose of this work is to investigate the origin of catalytic activity in the CO oxidation on $Mn_5Co_1O_x$ catalysts depending on the preparation temperature. High-resolution transmission electron microscopy (HRTEM), X-ray photoelectron spectroscopy (XPS), X-ray diffraction (XRD), N_2 physisorption, and temperature-programmed reduction in hydrogen (TPR-H_2) techniques were used to study the structure as well as the redox and surface properties of the catalysts.

2 Materials and Methods

The sample with the Co:Mn = 1:5 ratio was prepared by coprecipitation method. The calculated amount of $Co(NO_3)_2$ and $Mn(NO_3)_2$ aqueous solutions was poured into a round-bottom flask. Precipitation was carried out under stirring with a gradual addition of a NaOH aqueous solution to bring the pH of the solution to 11. After a subsequent aging, the precipitate was filtered, washed with distilled water on a filter to pH 6, and dried at 120 °C. The sample was calcined in air at 400, 600 or 800 °C for 4 h.

The phase composition was studied by XRD using a D8 Advance diffractometer (Bruker) equipped with a Lynxeye linear detector. The diffraction patterns were obtained in the 2θ range from 15° to 70° with a step of 0.05°, 7 s at each point using monochromatic Cu Kα radiation (λ = 1.5418 Å). The phases were identified using the powder diffraction database PDF-4+. The crystal size was estimated by the Scherrer formula using the most intensive reflection. The quantitative content of phases and structural parameters in the samples were found by the Rietveld method using the TOPAS software. A high resolution synchrotron radiation X-ray powder diffraction (SR-XRD) study was carried out on the I11 beamline at the Diamond Light Source, UK, with a photon energy of 15 keV (λ = 0.82449 Å).

The specific surface area was calculated with the Brunauer–Emmett–Teller (BET) method using nitrogen adsorption isotherms measured at liquid nitrogen

temperatures with an automatic Micromeritics ASAP 2400 sorptometer.

In situ XRD study was carried out under a flow of 10% H_2 in He on the same D8 Advance diffractometer equipped with a reaction chamber XRK-900 (Anton Paar). The total flow rate was 100 ml/min; the heating rate was 12 °C/min. The temperature increased from 175 to 700 °C with a step of 25 °C. XRD patterns were recorded at each temperature in the 2θ range from 28° to 50° with a step of 0.05°, 7 s at a point (52 min for a scan). Isothermal reduction was studied at 225 °C in the 2θ range from 21° to 46° (58 min for a scan).

The concentrations of manganese and cobalt ions in the solid solutions (Mn,Co)O and $(Mn,Co)_3O_4$ were calculated using the linearly approximated dependence of the lattice parameter or the unit cell volume on the Mn:Co ratio based on the literature data for CoO [JCPDS no. 43-1004], MnO [JCPDS no. 07-0230], $CoMn_2O_4$ [ICSD no. 39197], and Mn_3O_4 [JCPDS no. 18-0408].

HRTEM images were obtained using a JEM-2010 microscope (JEOL) with a resolution of 1.4 Å. Energy dispersive X-ray (EDX) analysis was carried out on an energy dispersive spectrometer XFlash with an energy resolution of 128 eV.

The temperature-programmed reduction in hydrogen was performed with 40–60 mg of the sample in a quartz reactor using a flow setup with a thermal conductivity detector. The reducing mixture (10 vol% of H_2 in Ar) was fed at 40 ml/min. The sample was heated from room temperature to 900 °C with a constant rate of approximately 10 °C/min.

XPS analysis was performed on an X-ray photoelectron spectrometer (SPECS Surface Nano Analysis GmbH, Germany) equipped with a XR-50 M X-ray source having a twin Al/Ag anode, a FOCUS-500 X-ray monochromator, and a PHOIBOS-150 hemispherical electron energy analyzer. The core-level spectra were obtained using monochromatic Al Kα radiation (hν = 1486.74 eV) under ultrahigh vacuum conditions. The charge correction was performed by setting the C1s peak at 284.8 eV. Relative concentrations of elements were determined from the integrated intensities of the core-level spectra using the cross sections according to Scofield [19]. For detailed analysis, the spectra were fitted into several peaks after the background subtraction by the Shirley method [20]. The fitting procedure was performed using the CasaXPS software (www.casaxps.com). The line shapes were approximated by the multiplication of Gaussian and Lorentzian functions.

Catalytic tests were performed in a flow regime in a glass reactor 170 mm in length and 10 mm in the inner diameter. The initial gas mixture composition was 1 vol% CO in air. The contact time was 0.12 s. All the samples were investigated in the temperature range 50–350 °C. A catalyst fraction of 0.4–1.0 mm was used. To avoid overheating during the exothermic reaction, the catalyst was mixed with a

quartz powder. The reactant mixture before and after the reactor was analyzed by a gas chromatograph equipped with a zeolite CaA column and a thermal conductivity detector.

Catalytic activity was calculated from the CO conversion at different flow rates (contact time was 0.08 and 0.24 s), taking into account the catalyst mass, according to the formula:

$$r(CO) = [C_o - C_{cur}] \cdot V/(60 \cdot m_{cat}), \quad [cm^3(CO)/g\,s]$$

$$C_{cur} = C_o \cdot (1 - ((P_0 - P_{cur}/P_0)),$$

where P_0 is the peak area corresponding to the initial concentration of CO in the reactant mixture; P_{cur} is the peak area corresponding to the current concentration of CO at the reactor outlet; C_{cur} is the current concentration of CO in the mixture, vol%; C_0 is the initial concentration of CO in the mixture ($C_0 = 1$ vol%); V is the feed rate of the reactant mixture, ml/min; and m_{cat} is the mass of the catalyst, g.

To compare the samples, their activities must be extrapolated to the same conversion of CO (in our case, 50% conversion):

$$r(CO)_{50\%} = 0.5 \times r/C_{cur}^{av}, \quad \text{where } C_{cur}^{av} = (C_o + C_{cur})/2, \quad (\%)$$

The reaction order for CO was taken equal to 1.

3 Results

3.1 Catalytic Tests in CO Oxidation

Figure 1 shows the evolution of CO conversion as a function of temperature for $Mn_5Co_1O_x$ catalysts prepared at 400, 600, and 800 °C. One can see that the low-temperature $Mn_5Co_1O_x$ catalyst calcined at 400 °C exhibits the best activity. There is a shift of the light-off curves toward low temperatures with decreasing the calcination temperature. The temperature of 50% CO conversion grows from 183 to 461 °C when the calcination temperature increases from 400 to 800 °C. The activation energy is 49, 56, and 67 kJ/mol for the catalysts synthesized at 400, 600, and 800 °C, respectively. The rates of CO oxidation normalized per mass and the specific surface area are listed in Table 1. We can see that both parameters decline with the calcination temperature. Differences in the activation energy and the rate of CO oxidation per specific surface area indicate the presence of various active sites in the catalysts. To elucidate the nature of active components, we will further investigate the catalysts by physical–chemical methods.

3.2 XRD and BET Analysis of As-Prepared Catalysts

The X-ray diffraction patterns of the synthesized samples are shown in Fig. 2a, experimental peaks correspond to a
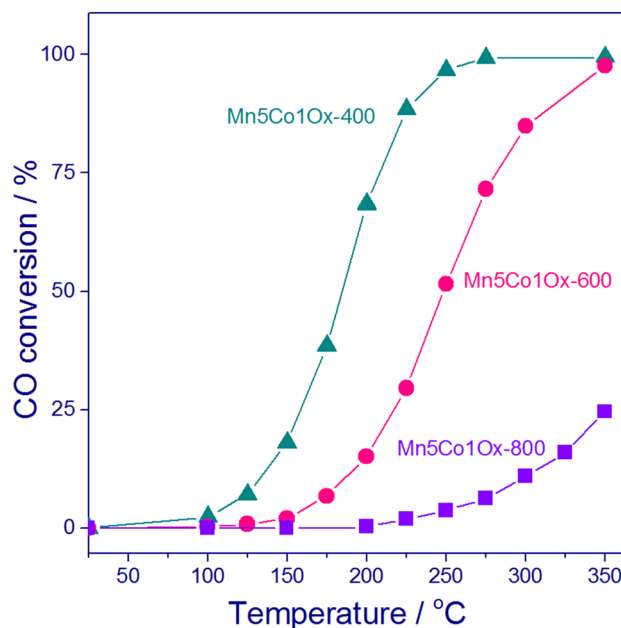

Fig. 1 CO oxidation conversion for $Mn_5Co_1O_x$ catalysts calcined at 400, 600, and 800 °C

Table 1 Catalytic activities (rate of CO oxidation at 250 °C) normalized per mass (r1) and specific surface area (r2) and activation energies (E_a)

Catalyst	r1 ($cm^3/(g \cdot s)$)	r2 ($cm^3/(m^2\,s)$)	E_a (kJ/mol)
$Mn_5Co_1O_x$-400	0.2376	0.0040	49
$Mn_5Co_1O_x$-600	0.0528	0.0025	56
$Mn_5Co_1O_x$-800	0.0030	0.0003	67

mixed Mn–Co oxide with the tetragonal spinel structure ($Mn_{3-x}Co_xO_4$). An increase in the calcination temperature from 400 to 800 °C leads to narrowing of the XRD peaks. The crystallite size of spinel grows from 230 to 530 Å. The specific surface area of the catalysts decreases from 60 to 10 m^2/g with increasing the calcination temperature, which is consistent with the change in the crystallite size. In the case of catalyst prepared at 400 °C, besides spinel reflections, broad peaks at $2\theta = 24.75°$ and $42.00°$ are also observed.

To obtain detailed information about phase composition of $Mn_5Co_1O_x$-400, the SR-XRD experiment with high intensity of incident beam was performed (Fig. 2b). SR-XRD reveals that these peaks correspond to 012, 104, $2\bar{1}3$, 024, $2\bar{1}6$, and $3\bar{1}4$ reflections of $CoMnO_3$ [ICSD no. 31854]. The phase quantification by the Rietveld refinement gave approximately 30% of $CoMnO_3$ and 70% of a $Co_xMn_{3-x}O_4$ spinel.

The volume of the spinel lattice increases from 306.4 to 308.8 $Å^3$ (Table 2) with increasing the calcination temperature and changes in comparison with Mn_3O_4 (313.38 Å,
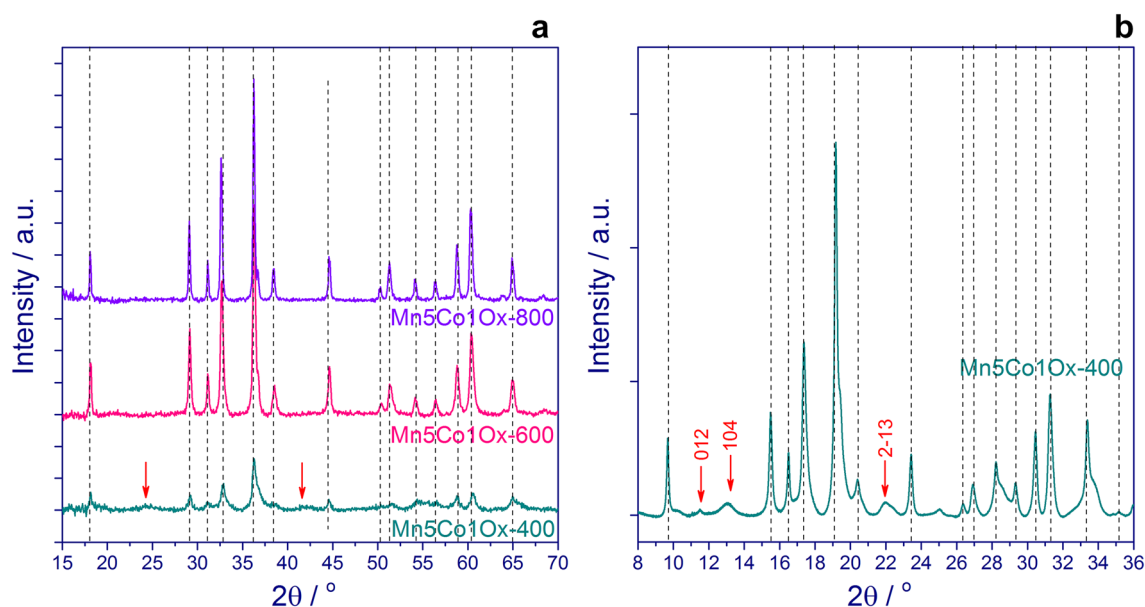
Fig. 2 XRD patterns of $Mn_5Co_1O_x$-400, $Mn_5Co_1O_x$-600, and $Mn_5Co_1O_x$-800 catalysts, $\lambda = 1.5418$ Å (**a**). SR-XRD of $Mn_5Co_1O_x$-400 (**b**), $\lambda = 0.82449$ Å. Dotted lines indicate the position of Mn_3O_4 tetragonal spinel reflections, arrows point to $CoMnO_3$ reflections

Table 2 Catalysts characterization data

Catalyst	Phase composition (wt%)	Lattice parameters, Å (volume, Å^3)	Crystallite size (Å)	S_{BET} (m^2/g)	T_{max} (°C)	H_2 consumption (mmol(H_2)/g)	Reduction degree (%)
$Mn_5Co_1O_x$-400	30% $CoMnO_3$	–	40	60	270	1.57	120
					335	3.28	
	70% $Co_xMn_{3-x}O_4$[a]	a = 5.740(2)	230		410	1.61	
		c = 9.300(9)			735	1.87	
		V = 306.4(5)					
$Mn_5Co_1O_x$-600	$Co_xMn_{3-x}O_4$[a]	a = 5.741(2)	320	21	210	0.07	102
		c = 9.341(7)			255	0.17	
		V = 307.8(5)			405	2.85	
					440	1.48	
					755	2.01	
$Mn_5Co_1O_x$-800	$Co_xMn_{3-x}O_4$[a]	a = 5.742(2)	530	10	470	3.91	91
		c = 9.366(7)			755	1.93	
		V = 308.8(5)					

[a] A solid solution $Co_xMn_{3-x}O_4$ based on the tetragonal spinel Mn_3O_4 structure

JCPDS no. 18-0408). There are several possible explanations of the lattice parameter change. On the one hand, Co cations can enter into the structure of Mn_3O_4, forming a $Co_xMn_{3-x}O_4$ solid solution. The observed values of the lattice volume are between pure Mn_3O_4 (313.38 Å^3, JCPDS no. 18-0408) and Mn_2CoO_4 (304.14 Å^3, ICSD no. 39,197), which can indicate the incorporation of cobalt cations into the Mn_3O_4 lattice. On the other hand, the change in the lattice volume may be due to lattice distortion, formation of cation vacancies or, in other words, the presence of excess

oxygen in $Co_xMn_{3-x}O_{4+\delta}$, as it is usually observed for low-temperature spinels [21].

For catalysts prepared at 600–800 °C, an estimation of the Co content in the spinel lattice on the basis of the Vegard rule showed that *x* is approximately equal to 0.5–0.6 in $Mn_{3-x}Co_xO_4$, which is close to the initial composition and indicates complete interaction between elements during the synthesis. In the case of $Mn_5Co_1O_x$-400, besides $Mn_{3-x}Co_xO_4$ spinel, 30% of $CoMnO_3$ is formed. Estimation of the spinel composition from mass balance gives

the composition of $Co_{0.1}Mn_{2.9}O_4$. On the other hand, according to the Vegard rule, the observed lattice volume $V = 306.4$ Å^3 corresponds to another content, $Co_{0.8}Mn_{2.2}O_4$. These differences indicate the presence of excess oxygen in $Co_{0.1}Mn_{2.9}O_{4+\delta}$ in comparison with the stoichiometric ratio $(Co + Mn):O = 3:4$ [21, 22]. Since the spinel structure has the closest oxygen packing, the presence of additional oxygen should indicate the occurrence of defects—cationic vacancies and the oxidation of Mn and/or Co cations (an increase in the Mn^{3+}/Mn^{2+} ratio in comparison with the stoichiometric one or the formation of Mn^{4+}/Co^{3+} ions). As discussed before, the appearance of cation vacancies and the change in the cation oxidation state affect the lattice parameters of the oxide.

3.3 TEM Study

The catalysts were studied by high-resolution transmission electron microscopy coupled with energy dispersive X-ray analysis. The results for the $Mn_5Co_1O_x$-400 catalyst are presented in Fig. 3. There are two types of particles: (1) massive rounded particles of 100–200 nm, which contain pores with sizes of 10–20 nm; (2) needle-shaped flat particles with a diameter of 10 nm and a length of 100 nm. The first type of particles consists of crystals with a size of 20 nm (Fig. 3b). The interplanar distance is 4.82 Å, which corresponds to (110) plane of Mn_3O_4 (Fig. 3c). EDX analysis in several points indicates that the atomic ratio between Mn and Co is 80:20. Rounded particles are covered with needle particles (Fig. 3d) with a characteristic interplanar distance d = 4.52 Å, which corresponds to (012) plane of $CoMnO_3$. These particles are degraded under the electron beam. EDX spectra from this point show that the atomic ratio Mn:Co is 70:30. It can be considered that this phase is unstable under the electron beam due to the vacancy nature.

In the case of the $Mn_5Co_1O_x$-800 catalyst, the needle particles disappear and the size of the massive round particles increases to 200–300 nm (Fig. 4a). The crystallinity increases and the crystallite size of primary particles increases to 50–100 nm (Fig. 4b). According to EDX analysis, the catalyst contains 75 at.% of Mn and 25 at.% of Co, which is in good agreement with the initial composition.
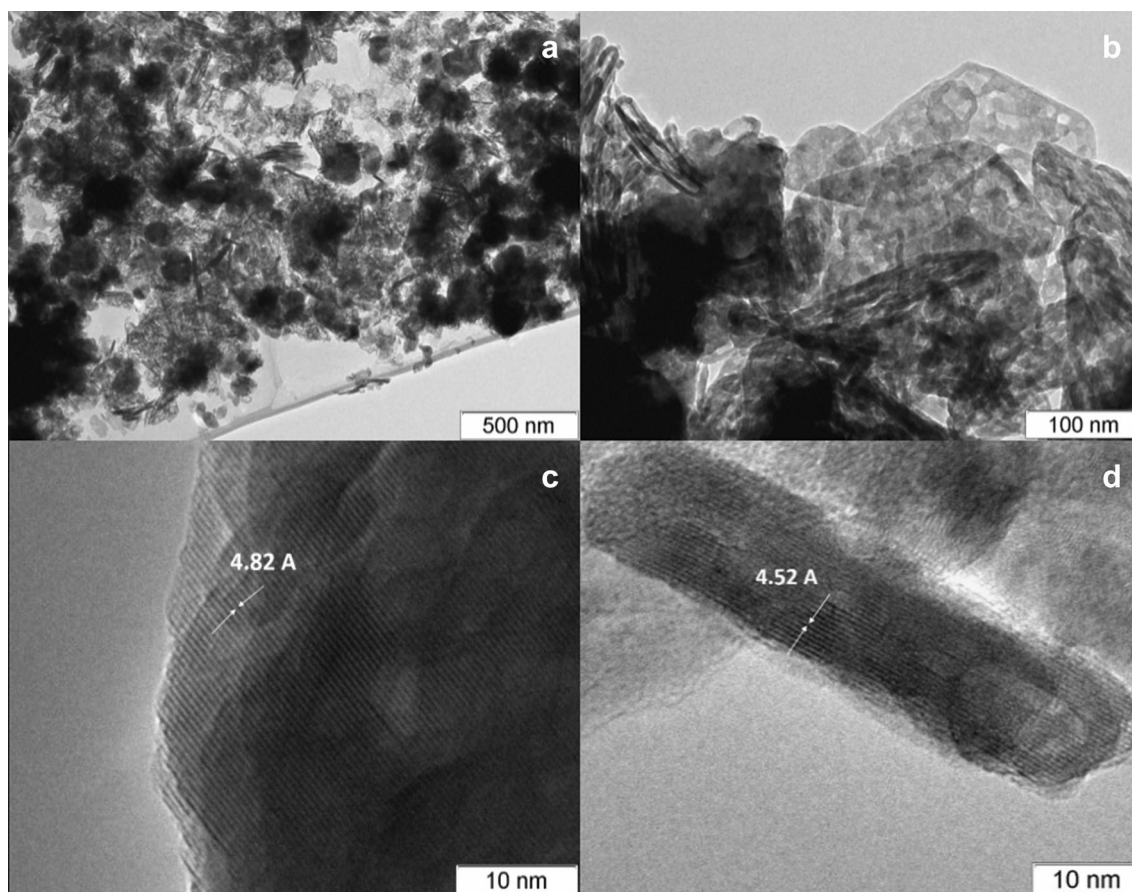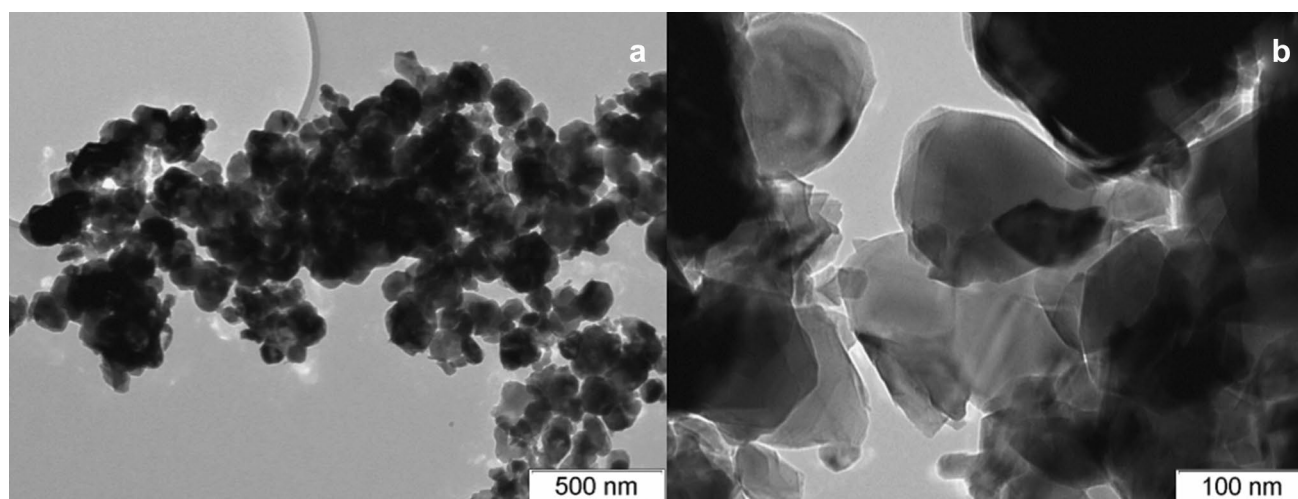

Fig. 3 TEM images of $Mn_5Co_1O_x$-400

Fig. 4 TEM images of $Mn_5Co_1O_x$-800

3.4 XPS Study

The relative concentrations (atomic ratios) of elements in the near-surface layer of the catalysts estimated by XPS as well as the $Mn2p_{3/2}$, $Co2p_{3/2}$, and $O1s$ binding energies are listed in Table 3. The atomic ratio [Co]/[Mn] in all the samples is in the range of 0.138–0.153, which is close to the value of 0.2 from the chemical composition.

Figure 5 shows the $Mn2p$ and $Co2p$ spectra of manganese oxides. The $Mn2p$ spectrum is represented by the $Mn2p_{3/2}$–$Mn2p_{1/2}$ spin-orbital doublet whose integrated intensity ratio is 2:1. To identify the chemical state of manganese, the $Mn2p_{3/2}$ binding energy is used as well as the presence and the position of the shake-up satellites, while the asymmetric shape of the main peaks of $Mn2p_{3/2}$ and $Mn2p_{1/2}$ is determined by multi-electron processes. The deconvolution of $Mn2p$ into individual components shows that the spectra of the studied samples are described

by three doublets $Mn2p_{3/2}$–$Mn2p_{1/2}$ and corresponding shake-up satellites. The $Mn2p_{3/2}$ peaks are observed at 640.0, 641.6, and 642.6 eV. In this case, two shake-up satellites exist at the first doublet, which are 4.7 and 7.3 eV away from the main peak. For the second doublet, one shake-up satellite is observed, which is 8.9 eV apart from the main peak. For the third doublet, two shake-up satellites are observed, which are 3.2 and 11.2 eV distant from the main peak. According to the literature, manganese in MnO, Mn_2O_3, and MnO_2 oxides is characterized by the $Mn2p_{3/2}$ binding energe in the ranges of 640.4–641.7, 641.5–641.9, and 642.2–642.6 eV, respectively [23–36]. Thus, the presence of manganese in the Mn^{2+}, Mn^{3+}, and Mn^{4+} states is observed in the $Mn_5Co_1O_x$ catalysts; the content of manganese in a different state is listed in Table 3. For $Mn_5Co_1O_x$-800, the largest amount of Mn^{4+} (48%) and the smallest amount of Mn^{2+} (5%) are observed, the calcination leads to an increase in the content of Mn^{2+}

Table 3 Atomic ratios of elements on the catalyst surface and the $Mn2p_{3/2}$, $Co2p_{3/2}$, and $O1s$ binding energies (eV)

Catalyst	$Mn2p_{3/2}$			$Co2p_{3/2}$	$O1s$, eV	[Co]/[Mn]	[O^a]/[Mn + Co]	[O]/[Mn + Co]
	Mn^{2+}, %	Mn^{3+}, %	Mn^{4+}, %	Co^{2+}, eV				
	640.0, eV	641.6, eV	642.4, eV					
$Mn_5Co_1O_x$-400	1	40	59	780.5	529.8 531.1^a	0.138	1.20	1.53
$Mn_5Co_1O_x$-600	15	65	20	780.5	529.9 531.2^a	0.136	1.21	1.52
$Mn_5Co_1O_x$-800	8	67	25	780.6	529.8 531.3^a	0.153	1.28	1.78

Oxygen belonging to the OH groups on the catalyst surface is presumably in the form of $Co(OH)_2$

[a]Oxygen with the $O1s$ binding energy at 529.8 eV

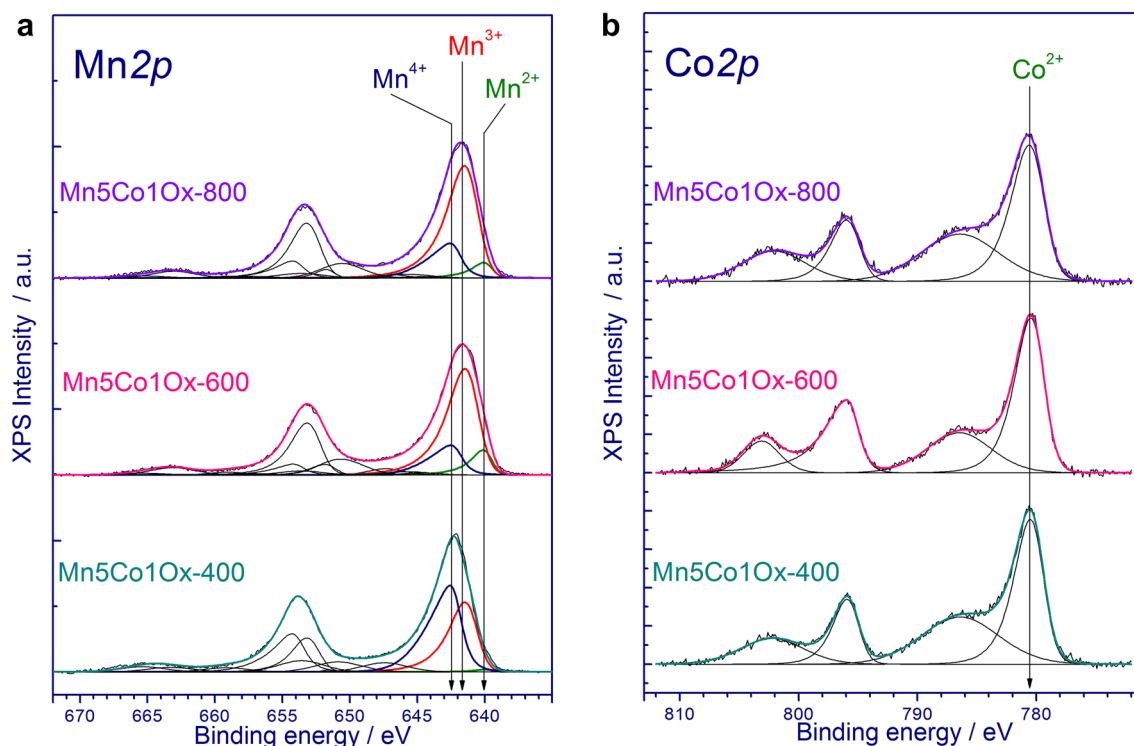**Fig. 5** Mn$2p$ (**a**) and Co$2p$ (**b**) spectra of the Mn$_5$Co$_1$O$_x$ catalyst. The Co$2p$ spectra are normalized to the integrated intensity of the corresponding Mn$2p$ spectra

and Mn^{3+}, which is probably due to the formation of the Co$_{0.5}$Mn$_{2.5}$O$_4$ solid solution with the spinel structure.

The Co2p spectra consist of the Co$2p_{3/2}$–Co$2p_{1/2}$ doublet, the integrated intensities of the components are correlated as 2:1 (Fig. 5). As for manganese, to identify the chemical state of cobalt, the position of the Co$2p_{3/2}$ main line, the shape of the Co$2p$ spectrum (the intensity and relative position of the "shake-up" satellites), and the spin–orbit splitting Co$2p_{3/2}$–Co$2p_{1/2}$ were used. The position and intensity of the "shake-up" satellite and the magnitude of the spin–orbit splitting depend on the chemical state of cobalt and on the chemical environment. In the case of Mn$_5$Co$_1$O$_x$ catalysts, the Co$2p_{3/2}$ spectra are represented by an asymmetric peak with a binding energy in the range of 780.4–780.6 eV and a broad "shake-up" satellite in the region of 786.6 eV corresponding to this line. The spin–orbit splitting of Co$2p_{3/2}$–Co$2p_{1/2}$ is 15.95 eV. In the spectrum of metallic cobalt Co^0 and oxides LiCoO$_2$ and Co$_3$O$_4$, intense shake-up satellites are not observed, and the binding energy Co$2p_{3/2}$ lies in the range of 778.0–778.2 and 779.5–780.5 eV [37–40]. Cobalt in the Co^{2+} state is characterized by Co$2p_{3/2}$ binding energies in the range of 780.0–782.0 and by the presence of an intense shake-up satellite in the range of 786–787 eV [37–39, 41, 42]. The value of the binding energy as well as the presence of a

low-intensity shake-up satellite indicate that cobalt is in the Co^{2+} state in the Mn$_5$Co$_1$O$_x$ catalysts.

3.5 TPR Study

Figure 6 shows the TPR curves of the Mn$_5$Co$_1$O$_x$ catalysts prepared at 400, 600, and 800 °C, as well as Mn$_3$O$_4$, Mn$_2$O$_3$, and Co$_3$O$_4$ used as reference samples. The reduction of Mn$_3$O$_4$ is characterized by one hydrogen absorption peak with a maximum at 550 °C due to Mn$_3$O$_4$ → MnO reduction, whereas Mn$_2$O$_3$ is characterized by two peaks at 400 and 465 °C, corresponding to the two-step reduction Mn$_2$O$_3$ → Mn$_3$O$_4$ → MnO [43, 44]. For Co$_3$O$_4$, there are two TPR peaks with the maxima at 270 and 320 °C. The presence of two peaks corresponds to the two-step reduction process: Co$_3$O$_4$ + H$_2$ → 3CoO + H$_2$O; CoO + H$_2$ → Co + H$_2$O [45–47].

The reduction of Mn$_5$Co$_1$O$_x$ differs essentially from the reduction of reference oxides. The observed differences are primarily associated with the appearance of high-temperature TPR peaks for all the Mn$_5$Co$_1$O$_x$ catalysts, which is due to reduction of (Mn,Co)O to Co and MnO [48]. Moreover, the TPR profiles of the Mn$_5$Co$_1$O$_x$ catalysts are significantly different (Fig. 6). The Mn$_5$Co$_1$O$_x$-400 catalyst is
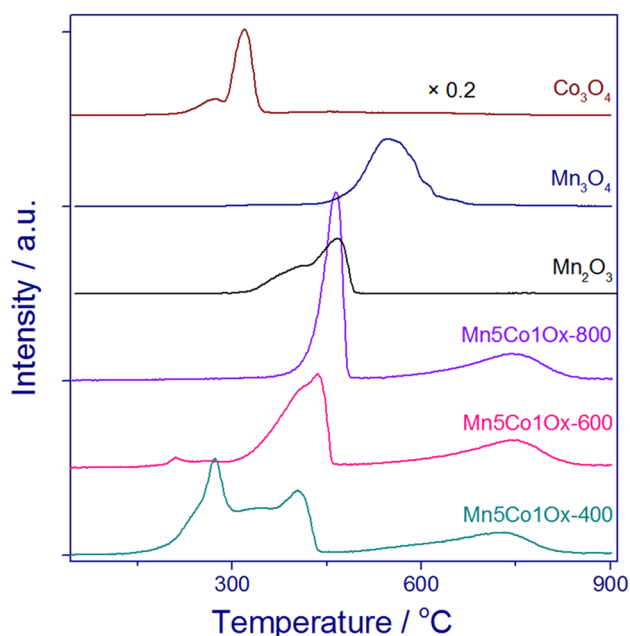
Fig. 6 TPR profiles of $Mn_5Co_1O_x$-400, $Mn_5Co_1O_x$-600, $Mn_5Co_1O_x$-800 catalysts and Mn_3O_4, Mn_2O_3, and Co_3O_4 reference samples

characterized by the appearance of intensive low-temperature peaks at 270 and 335 °C, in contrast to other catalysts.

For all the catalysts, there are two regions of the H_2 consumption: the low-temperature peaks located at 150–500 °C and a broad high-temperature peak between 500 and 850 °C. In the latter case, for all the catalysts, the position and the intensity of the high-temperature TPR peak are close (Table 1). The increase in the preparation temperature leads to a slight shift of the TPR profile to the high-temperature region. The temperature of TPR maximum increases from 735 to 750 °C. In the low-temperature region, the TPR profile of $Mn_5Co_1O_x$-800 contains only one peak with a maximum at 470 °C. For $Mn_5Co_1O_x$-600, this peak becomes wide and splits into two peaks with the maxima at 405 and 440 °C and intensity 2.85 and 1.48 mmol(H_2)/g. Moreover, small low-temperature TPR peaks at 210 and 255 °C appear. In the case of $Mn_5Co_1O_x$-400, intensity of the low-temperature peaks grows, first and second TPR peaks at 270 and 335 °C contain 58% of the total consumption of H_2.

Our previous study reveals that the reduction of the well crystalline $(Mn,Co)_3O_4$ spinel prepared at 800 °C goes in two steps. The first TPR peak corresponds to the transformation of $(Mn,Co)_3O_4$ to $(Mn,Co)O$. The second TPR peak is due to the reduction of $(Mn,Co)O$ to metallic Co and MnO [48]. For $Mn_5Co_1O_x$-800, the ratio between first and second TPR peaks is 2:1, which corresponds to the two reduction reactions $Co_{0.5}Mn_{2.5}O_4 + H_2 \rightarrow 3Mn_{0.83}Co_{0.17}O + H_2O$ and $Mn_{0.83}Co_{0.17}O + 0.17H_2 \rightarrow 0.83MnO + 0.17Co + 0.17H_2O$. For $Mn_5Co_1O_x$-400 and $Mn_5Co_1O_x$-600, the appearance of

low-temperature peaks could be assigned to the reduction of easily reducible species such as Mn^{4+} [10]. According to XRD, $Mn_5Co_1O_x$-400 contains 30 wt% of $MnCoO_3$, which contains Mn^{4+}. For all the catalyst, the degree of reduction was estimated under the assumption that the reduction product contains only Co and MnO. For $Mn_5Co_1O_x$-800 and $Mn_5Co_1O_x$-600, the reduction degree is 91–102%; however, in the case of the low-temperature $Mn_5Co_1O_x$-400 catalyst, it reaches 120% (the degree of reduction was estimated under the assumption that $Co_{0.1}Mn_{2.9}O_4 + CoMnO_3$ transforms to Co and MnO). The reduction degree over 100% for $Mn_5Co_1O_x$-400 indicates that there are some easy reducible species, which we did not calculate. Probably, it could be due to a loss of excess oxygen in $Co_xMn_{3-x}O_{4+\delta} \rightarrow Co_xMn_{3-x}O_4$ and reduction of $Mn^{4+} \rightarrow Mn^{3+}$ or $Mn^{3+} \rightarrow Mn^{2+}$ or $Co^{3+} \rightarrow Co^{2+}$ in the bulk of a solid solution. It can be assumed that the low-temperature TPR peaks at 150–350 °C are due to the reduction of excess oxygen from $Co_xMn_{3-x}O_{4+\delta}$ and $MnCoO_3$ oxides.

3.6 In Situ XRD Study

The phase transformations that occur during the reduction of $Mn_5Co_1O_x$-400 catalyst have been further studied by in situ XRD. In these experiments, the XRD patterns were collected during the stepwise heating of the samples in 10%H_2 in the He mixture from room temperature to 700 °C. The results of the investigation of $Mn_5Co_1O_x$-400 are presented in Fig. 7. At room temperature, the catalyst consists of oxides with the tetragonal spinel structure, such as $Mn_{3-x}Co_xO_4$ and $CoMnO_3$. At 250 °C, the 113 diffraction peak of $CoMnO_3$ disappears. Above 300 °C, the intensity of spinel reflections declines and wide peaks appear at approximately 35.3° and 41°, corresponding to 200 and 111 reflections of a MnO-like oxide. At 575 °C, a new line appears at 44° corresponding to metallic cobalt, and the intensity of a MnO-like intermediate compound decreases. At 575–700 °C, the reflections of Co and the MnO-like oxide are observed.

To estimate lattice parameters of the intermediate oxides without thermal expansion, the sample was cooled from 625 °C to RT. The lattice parameter is 4.418(1) Å, which differs from the literature data for MnO (4.445 Å, JCPDS no. 07-0230) and CoO (4.260 Å, JCPDS no. 431004). Such change in the lattice parameter indicates the formation of a $Mn_{1-x}Co_xO$ solid solution. The composition of solid solutions was estimated using the Vegard rule. The composition of the intermediate state corresponds to $Mn_{0.85}Co_{0.15}O$. After reduction at 700 °C, the lattice parameter becomes 4.443(1) Å, indicating the formation of MnO. According to the fraction weigh estimation, which was performed by the Rietveld refinement, the reduction product contains 12 wt% of Co and 88 wt% of MnO. During the reduction, Co cations leave the $Mn_{0.85}Co_{0.15}O$ solid solution and form metallic Co.

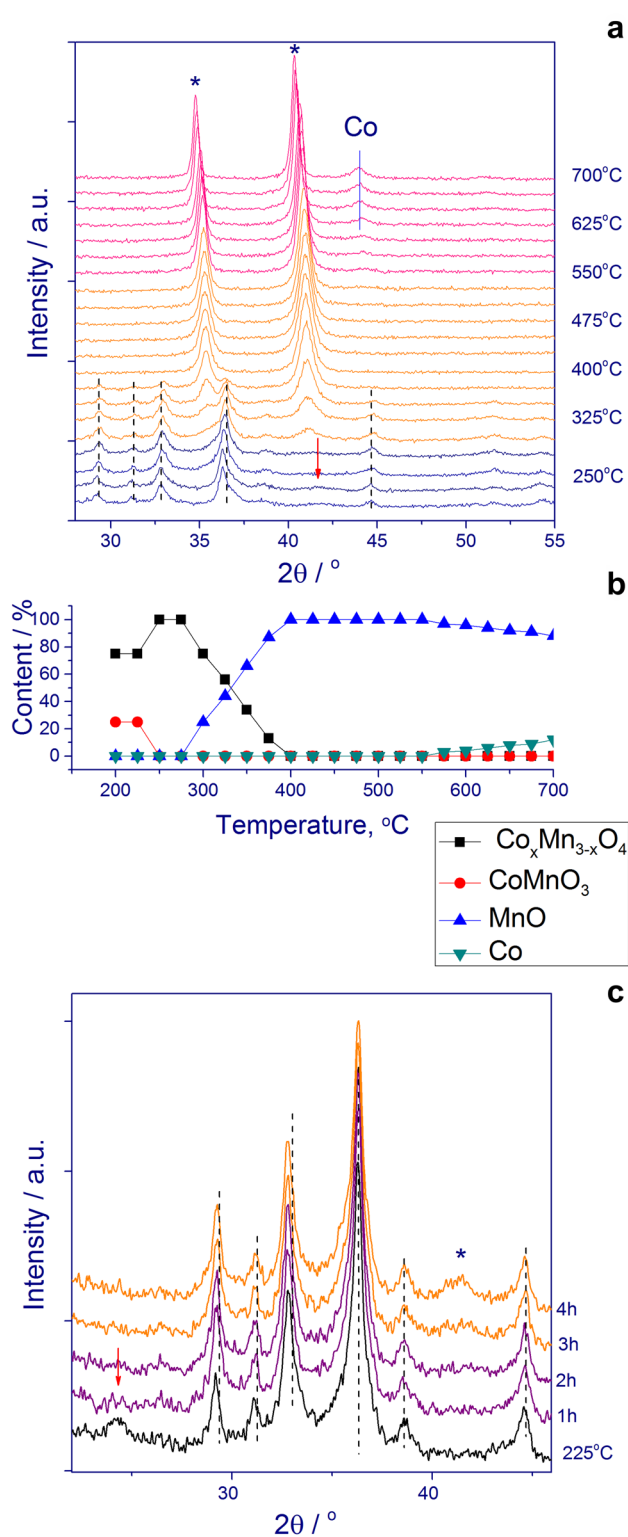**Fig. 7** In situ XRD patterns of $Mn_5Co_1O_x$-400 collected during heating from 200 to 700 °C in a flow of 10%H_2 in He gas mixture (**a**), quantitative phase composition as a function of the reduction temperature (**b**), and isothermal reduction at 225 °C (**c**). Dotted lines indicate the position of Mn_3O_4 tetragonal spinel reflections, arrows point to $CoMnO_3$ reflections, solid line—Co, *—(Mn,Co)O

In addition, the isothermal reduction at 225 °C was investigated (Fig. 7c). At the beginning, the reflection of $MnCoO_3$ disappears and after three scans the formation of the MnO-like oxide is observed.

4 Discussion

Despite the abundance of work in this area, the nature of the synergistic effect with respect to catalytic activity is not completely clear. On the one hand, the synergistic effect is associated with the formation of mixed oxides having the spinel structure [11]; on the other hand, the formation of highly dispersed or amorphous oxides was observed [15]. In this work, the most active Co–Mn catalyst was obtained at a relatively low temperature of 400 °C, at which incomplete interaction between elements and the formation of dispersed particles are possible. According to XRD, for all the $Mn_5Co_1O_x$ catalysts, the presence of $Mn_{3-x}Co_xO_4$ with tetragonal spinel structure was observed. For $Mn_5Co_1O_x$-400, SR-XRD revealed the formation of highly disperse $CoMnO_3$ particles, in which Mn cations are in the Mn^{4+} state. The XPS results show the formation of Mn^{4+} on the surface for the most active catalyst. The calcination temperature greatly affects the specific surface area, the crystallite size, phase composition and morphology. At 400 °C, poorly crystalline oxides, such as $CoMnO_3$ and $Mn_{3-x}Co_xO_{4+\delta}$, are formed. Mixed oxides are transformed into well crystalline spinel $Mn_{2.5}Co_{0.5}O_4$ when the calcination temperature is increased to 800 °C. The calcination temperature changes the redox properties of the catalysts. $Mn_5Co_1O_x$-800 is characterized by a high-temperature reduction of mixed oxide: $Co_{0.5}Mn_{2.5}O_4 \rightarrow Mn_{0.85}Co_{0.15}O \rightarrow MnO + Co$. While for $Mn_5Co_1O_x$-400, the low-temperature reducibility is connected with the formation of $Mn_{3-x}Co_xO_{4+\delta}$ with excess oxygen and $CoMnO_3$.

It is generally reported that many parameters, such as specific surface area, crystallite size, pore system, reducibility of Mn–Co species or oxygen mobility, and active oxygen species, are relevant to the good activity of Mn–Co oxide based catalysts for oxidation reactions [10–12, 14, 16–18]. In our work, we observed the catalytic activity in CO oxidation to increase with the specific surface area, the change in active species, the formation of $MnCoO_3$, the total amount of H_2 consumption, the presence of Mn^{4+} and the low-temperature reducibility.

5 Conclusions

A series of $Mn_5Co_1O_x$ catalysts calcined at different temperatures in the range of 400–800 °C were synthesized by coprecipitaion of manganese and cobalt nitrates. Their

catalytic performance were tested in the oxidation of CO. The low-temperature catalyst calcined at 400 °C displays the best catalytic activity, which is attributed to its high surface area, low-temperature reducibility, and a high surface concentration of Mn^{4+}. The formation of highly disperse and active $CoMnO_3$ species and excess oxygen in a $Mn_{3-x}Co_xO_{4+\delta}$ spinel leads to excellent low-temperature redox properties. The elevated temperature calcination results in the decline in the catalytic activity in CO oxidation due to formation of a well crystalline $Mn_{3-x}Co_xO_4$ spinel, a decrease in the surface area and reducibility.

Compliance with Ethical Standards

Conflict of interest The authors declare that they have no conflict of interest.

Ethical Approval This article does not contain any studies involving human participants performed by any of the authors.

References

1. Tomatis M, Xu HH, He J, Zhang XD (2016) Recent development of catalysts for removal of volatile organic compounds in flue gas by combustion: a review. J Chem 2016:8324826
2. Kamal MS, Razzak SA, Hossain MM (2016) Catalytic oxidation of volatile organic compounds (VOCs)—a review. Atmos Environ 140:117–134
3. Huang H, Xu Y, Feng Q, Leung DYC (2015) Low temperature catalytic oxidation of volatile organic compounds: a review. Catal Sci Technol 5:2649–2669
4. Liotta LF (2010) Catalytic oxidation of volatile organic compounds on supported noble metals. Appl Catal B 100:403–412
5. Royer S, Duprez D (2011) Catalytic oxidation of carbon monoxide over transition metal oxides. ChemCatChem 3:24–65
6. Fedorov AV, Tsapina AM, Bulavchenko OA, Saraev AA, Odegova GV, Ermakov DY, Zubavichus YV, Yakovlev VA, Kaichev VV (2018) Structure and chemistry of Cu–Fe–Al nanocomposite catalysts for CO oxidation. Catal Lett 148:3715–3722
7. Shi J (2013) On the synergetic catalytic effect in heterogeneous nanocomposite catalysts. Chem Rev 113:2139–2181
8. Xu H, Yan N, Qu Z, Liu W, Mei J, Huang W et al (2017) Gaseous heterogeneous catalytic reactions over Mn-based oxides for environmental applications: a critical review. Environ Sci Technol 51:8879–8892
9. Tian ZY, Tchoua Ngamou PH, Vannier V, Kohse-Höinghaus K, Bahlawane N (2012) Catalytic oxidation of VOCs over mixed Co-Mn oxides. Appl Catal B 117–118:125–134
10. Zhang X, Junhui Y, Jing Y, Ting C, Bei X, Zhe L et al (2018) Excellent low-temperature catalytic performance of nanosheet Co-Mn oxides for total benzene oxidation. Appl Catal A 566:104–112
11. Tang W, Wu X, Li S, Li W, Chen Y (2014) Porous Mn–Co mixed oxide nanorod as a novel catalyst with enhanced catalytic activity for removal of VOCs. Catal Commun 56:134–138
12. Qu Z, Gao K, Fu Q, Qin Y (2014) Low-temperature catalytic oxidation of toluene over nanocrystal-like Mn–Co oxides prepared by two-step hydrothermal method. Catal Commun 52:31–35
13. Lamonier JF, Boutoundou AB, Gennequin C, Pérez-Zurita MJ, Siffert S, Aboukais A (2007) Catalytic removal of toluene in air over Co-Mn-Al nano-oxides synthesized by hydrotalcite route. Catal Lett 118:165–172
14. Kovanda F, Rojka T, Dobešová J, Machovič V, Bezdička P, Obalová L et al (2006) Mixed oxides obtained from Co and Mn containing layered double hydroxides: preparation, characterization, and catalytic properties. J Solid State Chem 179:812–823
15. Aguilera DA, Perez A, Molina R, Moreno S (2011) Cu-Mn and Co-Mn catalysts synthesized from hydrotalcites and their use in the oxidation of VOCs. Appl Catal B 104:144–150
16. Faure B, Alphonse P (2015) Co-Mn-oxide spinel catalysts for CO and propane oxidation at mild temperature. Appl Catal B 180:715–725
17. Liu C, Gong L, Dai R, Lu M, Sun T, Liu Q et al (2017) Mesoporous Mn promoted Co$_3$O$_4$ oxides as an efficient and stable catalyst for low temperature oxidation of CO. Solid State Sci 71:69–74
18. Wu M, Zhan W, Guo Y, Guo Y, Wang Y, Wang L et al (2016) An effective Mn-Co mixed oxide catalyst for the solvent-free selective oxidation of cyclohexane with molecular oxygen. Appl Catal A 523:97–106
19. Scofield JH (1976) Hartree-Slater subshell photoionization cross-sections at 1254 and 1487 eV. J Electron Spectrosc Relat Phenom 8:129–137
20. Shirley DA (1972) High-resolution X-ray photoemission spectrum of the valence bands of gold. Phys Rev B 5:4709–4714
21. Venediktova OS, Bulavchenko OA, Afonasenko TN, Tsyrul'nikov PG, Vinokurov ZS, Chesalov YA et al (2017) Synthesis and characterization of mixed manganese-gallium oxides $Mn_{3-x}Ga_xO_4$ (x = 1–2) with the spinel structure. J Alloys Compd 725:496–503
22. Bulavchenko OA, Venediktova OS, Afonasenko TN, Tsyrul'nikov PG, Saraev AA, Kaichev VV et al (2018) Nonstoichiometric oxygen in Mn-Ga-O spinels: reduction features of the oxides and their catalytic activity. RSC Adv 8:11598–11607
23. Regan E, Groutso T, Metson JB, Steiner R, Ammundsen B, Hassell D et al (1999) Surface and bulk composition of lithium manganese oxides. Surf Interface Anal 27:1064–1068
24. Oku M, Hirokawa K, Ikeda S (1975) X-ray photoelectron spectroscopy of manganese–oxygen systems. J Electron Spectrosc Relat Phenom 7:465–473
25. Castro VD, Polzonetti G (1989) XPS study of MnO oxidation. J Electron Spectrosc Relat Phenom 48:117–123
26. Bondi JF, Oyler KD, Ke X, Schiffer P, Schaak RE (2008) Chemical synthesis of air-stable manganese nanoparticles. J Am Chem Soc 131:9144–9145
27. Han Y-F, Chen F, Zhong Z, Ramesh K, Chen L, Widjaja E (2006) Controlled synthesis, characterization, and catalytic properties of Mn$_2$O$_3$ and Mn$_3$O$_4$ nanoparticles supported on mesoporous silica SBA-15. J Phys Chem B 110:24450–24456
28. Han Y-F, Chen L, Ramesh K, Zhong Z, Chen F, Chin J et al (2008) Coral-like nanostructured a-Mn$_2$O$_3$ nanocrystals for catalytic combustion of methane part I. Preparation and characterization. Catal Today 131:35–41
29. Yang X, Wang X, Zhang G, Zheng J, Wang T, Liu X et al (2012) Enhanced electrocatalytic performance for methanol oxidation of Pt nanoparticles on Mn$_3$O$_4$-modified multi-walled carbon nanotubes. Int J Hydrogen Energy 37:11167–11175

30. Ramesh K, Chen L, Chen F, Liu Y, Wang Z, Han Y-F (2008) Re-investigating the CO oxidation mechanism over unsupported MnO, Mn_2O_3 and MnO_2 catalysts. Catal Today 131:477–482

31. Liu Y, Li J, Li W, Li Y, Chen Q, Zhan F (2015) Nitrogen-doped graphene aerogel-supported spinel $CoMn_2O_4$ nanoparticles as an efficient catalyst for oxygen reduction reaction. J Power Sources 299:492–500

32. Kong W, Gao B, Jiang C, Chang A (2015) Influence of the oxygen pressure on the preferred orientation and optical properties of the pulsed-laser deposited $Mn_{1.56}Co_{0.96}Ni_{0.48}O_4 \pm \delta$ thin films. J Alloys Compd 650:305–310

33. Zhang L, Tang Z, Wang S, Ding D, Chen M, Wan H (2012) Growth and vibrational properties of MnOx thin films on Rh(111). Surf Sci 606:1507–1511

34. Jadhav PR, Suryawanshi MP, Dalavi DS, Patil DS, Jo EA, Kolekar SS et al (2015) Design and electro-synthesis of 3-D nanofibers of MnO_2 thin films and their application in high performance supercapacitor. Electrochim Acta 176:523–532

35. Kostowskyj MA, Kirk DW, Thorpe SJ (2010) Ag and Ag–Mn nanowire catalysts for alkaline fuel cells. Int J Hydrogen Energy 35:5666–5672

36. Hishida T, Ohbayashi K, Saitoh T (2013) Hidden relationship between the electrical conductivity and the Mn 2p core-level photoemission spectra in $La_{1-x}Sr_xMnO_3$. J Appl Phys 113:043710

37. Khassin AA, Yurieva TM, Kaichev VV, Bukhtiyarov VI, Budneva AA, Paukshtis EA et al (2001) Metal–support interactions in cobalt-aluminum co-precipitated catalysts: XPS and CO adsorption studies. J Mol Catal A 175:189–204

38. Biesinger MC, Payne BP, Grosvenor AP, Lau LWM, Gerson AR, Smart RSC (2011) Resolving surface chemical states in XPS analysis of first row transition metals, oxides and hydroxides: Cr, Mn, Fe, Co and Ni. Appl Surf Sci 257:2717–2730

39. Venezia AM, Murania R, Pantaleo G, Deganello G (2007) Nature of cobalt active species in hydrodesulfurization catalysts: combined support and preparation method effects. J Mol Catal A 271:238–245

40. Kosova NV, Devyatkina ET, Kaichev VV (2007) Optimization of Ni^{2+}/Ni^{3+} ratio in layered Li (Ni, Mn, Co) O_2 cathodes for better electrochemistry. J Power Sources 174:965–969

41. Liu B, Chai Y, Li Y, Wang A, Liu Y, Liu C (2014) Effect of sulfidation atmosphere on the performance of the $CoMo/\gamma$-Al_2O_3 catalysts in hydrodesulfurization of FCC gasoline. Appl Catal A 471:70–79

42. Guan Q, Cheng J, Li X, Wang B, Huang L, Nie F et al (2015) Low temperature vacuum synthesis of triangular CoO nanocrystal/graphene nanosheets composites with enhanced lithium storage capacity. Sci Rep 5:10017

43. Stobbe ER, De Boer BA, Geus JW (1999) The reduction and oxidation behaviour of manganese oxides. Catal Today 47:161–167

44. Christel L, Pierre A, Abel DAMR (1997) Temperature programmed reduction studies of nickel manganite spinels. Thermochim Acta 306:51–59

45. Arnoldy P, Moulijn JA (1985) Temperature-programmed reduction of CoO Al_2O_3 catalysts. J Catal 93:38–54

46. Garces LJ, Hincapie B, Zerger R, Suib SL (2015) The effect of temperature and support on the reduction of cobalt oxide: an in situ X-ray diffraction study. J Phys Chem C 119:5484–5490

47. Bulavchenko OA, Cherepanova SV, Malakhov VV, Dovlitova LS, Ishchenko AV, Tsybulya SV (2009) In situ XRD study of nanocrystalline cobalt oxide reduction. Kinet Catal 50:192–198

48. Bulavchenko OA, Gerasimov EY, Afonasenko TN (2018) Reduction of double manganese-cobalt oxides: in situ XRD and TPR study. Dalton Trans 47:17153–17159